

Modeling, Simulation and Experimental Validation of a Tendon-driven Soft-arm Robot Configuration - A Continuum Mechanics Method

Nikolaos Charalamos Chairopoulos¹, Panagiotis Vartholomeos¹, and Evangelos Papadopoulos¹, *Fellow, IEEE*

Abstract—This paper presents the mathematical derivation and experimental validation of a computational model, which accurately predicts static, large-strain deformations of tendon driven non-slender soft-arm manipulators subjected to gravity. The large strain behaviors are captured by employing the Green-Lagrange strain and by deriving analytical expressions for the variation of the equivalent Young modulus of the structure due to the large strains. No simplifying assumptions are made regarding the curvature of the structure, the stretching or the compression. Furthermore the paper proposes an iterative method for numerically solving the resultant non-linear system of coupled differential equations and demonstrates a number of application scenarios. The model is experimentally validated using a set-up comprising one segment of tendon driven soft-arm, which integrates stretchable and compressible hyperelastic (rubber-type) materials into its non-homogeneous back bone structure.

I. INTRODUCTION

Soft robotic arms offer advantages over their rigid counterparts due to their large compliance, which enables shape flexibility, safe interaction with unstructured environment, and whole-arm manipulation capabilities. Due to these properties they lend themselves very well to applications that involve direct human robot interaction in small workspaces, such as those in surgical robotics, assistive robotics, wearable systems, and collaborative robots [1]. The structure of soft robotic manipulators is usually constructed by elastomers, springs, bellows, flexures or flexible beams, all of which exhibit large compliance, constituting of a theoretically infinite degree of freedom (dof) structure, while at the same time being actuated by a limited number of actuators [2], [3], resulting in an underactuated system. An example of tendon driven soft-arm is the I-Support dual arm whose concept is depicted in Fig. 1. This integrates stretchable and compressible hyperelastic (rubber-type) materials into its structure and is designed for assistive washing tasks for the elderly [4].

Previous efforts to model the mechanics of soft robotic arm motion may be categorised into three approaches: pure kinematic modeling, lumped parameter dynamic modeling and continuum mechanics modeling. Pure kinematic models (forward, inverse and differential) have been applied to tendon driven or pneumatically actuated multi-segment soft robotic arms [5], [6], [7]. They are based on the assumption of piecewise constant curvature (PCC) bending, which has

This work was partially funded by the I-Support HORIZON 2020 PHC-19 project, Grant Agreement no: 643666, <http://www.i-support-project.eu/>

The authors are with the School of Mechanical Engineering, National Technical University of Athens, Greece. Contact email: {egpapado, pvarthol}@central.ntua.gr, nikoschairop@gmail.com.

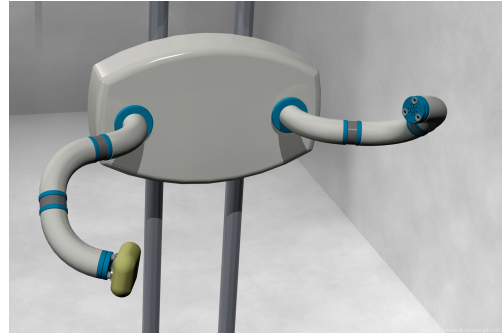


Fig. 1: I-Support dual soft-arm manipulators concept.

been validated by experiments and is very efficient in the absence of external loads, or when the external loads are small enough to not affect the curvature notably. Lumped parameter models are used to describe the dynamic response of the end-effector [3], [8], [9], [10], [11] and they have demonstrated accurate results. Continuum mechanics methods are based on distributed parameter models, which allow for an arbitrary soft arm deformation and shape generation in response to external loading. Cosserat's method has been used to represent flexible robot structures, with very high accuracy, as a one-dimensional curve in space with all relevant elastic, gravitational and actuation forces modeled as applied loading [10], [12], [13]. An Euler-Bernoulli model with the assumption of PCC was used in [14] to model the mechanics of concentric tubes. Energy-based models for the statics and dynamics of a planar continuum robot with in-plane loads have been presented in [15]. These models point out the importance of the internal strain energy in these structures. Also, accurate modeling of soft material is provided by Finite Element Methods (FEM) [16]. However, FEM are computationally demanding and are not considered an efficient solution for real-time model-based control.

The contribution of this paper is the derivation and validation of a computational model for static, large-strain deformations of tendon driven, soft-arm manipulators subjected to gravity. The large strain behaviors are captured by employing the Green-Lagrange strain and by taking into account the variation of the equivalent Young modulus of the structure due to the large strains. No simplifying assumptions are made regarding the curvature of the structure, the stretching or the compression. Making no assumptions on the curvature of the structure and the extensibility or compressibility yields a generic model that can be employed for predicting behaviors of multiscale soft robots subjected to gravity. The methodology presented in this paper refers to the 2-D large-strain problem, but can be extended to the 3-D case.

II. GENERIC TENDON DRIVEN SOFT-ARM DESCRIPTION

We consider the generic tendon driven soft-arm shown in Fig. 2. This arm is capable of performing 2D planar motions on the $x-y$ plane. The actuation comprises two antagonistic tendons which pass through two sheaths and connect the actuators' servomotor pulleys to the soft-arm end-effector cross-section. When the tendon forces T_1, T_2 are applied, axial compressive forces and bending moments appear. Fig. 2 shows a case where $T_1 > T_2$.

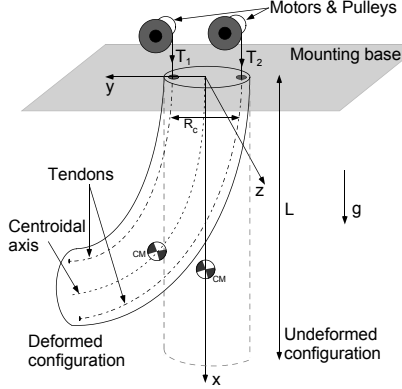


Fig. 2: I-Support soft-arm deformed and undeformed configuration.

Figure 3 depicts the free body diagram, the internal forces, and an infinitesimal element of the soft arm with antagonistic tendons. N is the axial force, M is the bending moment, and Q is the transverse shearing force, $d\phi$ is the angle of bending of the infinitesimal element, ds the length of the infinitesimal element, where s is a distance along the path of the centroidal axis, and dW is the weight of the differential element (see Fig. 3). Length l is the offset of the CM from the vertical x axis. Constant g is the acceleration of gravity.

The goal is to calculate the soft-arm static 2D configuration, when driven by known tendon forces $T_1(0), T_2(0)$, without making any assumption on the *curvature of the structure* and the *magnitude of the axial strain*. To this end, the horizontal and vertical deformation and the bending angle ϕ at every point of the centroidal axis have to be calculated, which in turn requires the calculation of the internal forces M, Q, N at each cross-section and the calculation of the tendon forces along the tendon path. If the deformation of the points on the centroidal axis is known, then the deformation of any point on the cross-section can be found too, (not shown in this paper due to economy of space). In order to solve for these unknowns, the ordinary differential equations (ODE) governing the static configuration of the soft arm are formulated and integrated for every discretized element on the centroidal. The next section derives these ODEs.

III. LARGE DEFLECTION MODELING OF SOFT-ARM

A. Modeling of tendon transmissions

For all belts, tendons, ropes etc., for small contact angles, and for impeding motion the following holds [17]:

$$\frac{dT_i(s)}{ds} = -\mu_s T_i(s) \frac{d\phi(s)}{ds} \quad (1)$$

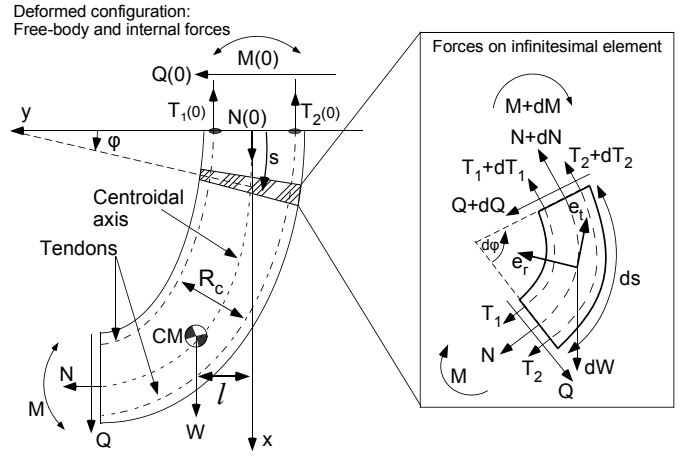


Fig. 3: Side view ($x-y$) of free-body diagram, internal forces, and infinitesimal element, of the soft-arm when actuated by 2 tendons.

where μ_s is the coefficient of static friction, and $i = \{1, 2\}$ denote the right and left tendon.

B. Infinitesimal element differential relationships

The equations of static equilibrium of forces along the tangential direction (index t), and radial direction, (index r), and of moments M about the Centre of Mass (CM) of the infinitesimal element of Fig. 3 are expressed in the radial and tangential components, and are given by:

$$\sum F_r = 0 \quad (2)$$

$$\sum F_t = 0 \quad (3)$$

$$\sum M = 0 \quad (4)$$

The gravity force dW is given by :

$$dW = \rho(s)gds \quad (5)$$

where $\rho(s)$ is the linear density. Due to structure non-homogeneity during deformations, ρ is a function of s .

Algebraic manipulations of (2)-(4) and cancellation of second order differentials, yield the relationship among differentials $dQ, dM, dN, dT_i, i = 1, 2$:

$$dQ = -T_1 d\phi - T_2 d\phi - Nd\phi - \sin(\phi)\rho(s)gs \quad (6)$$

$$dN = -dT_2 - dT_1 + Qd\phi + \cos(\phi)\rho(s)gds \quad (7)$$

$$dM = (dT_2 - dT_1)R_c + Qds \quad (8)$$

where R_c is the distance between the tendons of the soft arm, variables in (1), (6), (7) and (8) are functions of the variable s , as shown in the free-body diagram in Fig. 3. For integration purposes, it is more convenient to express all relationships as a function of the variable x , where x is the length on the undeformed centroidal axis. Therefore, a change of variable from s to x is performed in the next section.

C. Change of variables from s to x

In Fig. 4, $\{x_{Ai}, y_{Ai}\}$ and $\{x_{Bi}, y_{Bi}\}$ are the coordinates of points A and B in the undeformed state. When the arm is deformed, the same points are located in $\{x_{Af}, y_{Af}\}, \{x_{Bf}, y_{Bf}\}$. Vectors $\mathbf{u}_A, \mathbf{u}_B$ are the vertical displacement vectors and

w_A, w_B are the horizontal displacement vectors. Then ds is defined as the distance of A and B in the deformed state:

$$\begin{aligned} ds &= \left\| \begin{bmatrix} x_{Bf} - x_{Af} \\ y_{Bf} - y_{Af} \end{bmatrix} \right\| \\ &= \left\| \begin{bmatrix} (x_{Bi} + u_B) - (x_{Ai} + u_A) \\ w_B - w_A \end{bmatrix} \right\| \\ &= \left\| \begin{bmatrix} du + dx \\ dw \end{bmatrix} \right\| \end{aligned} \quad (9)$$

where

$$dx = x_{Bi} - x_{Ai} \quad (10)$$

$$du = u_B - u_A \quad (11)$$

$$dw = w_B - w_A \quad (12)$$

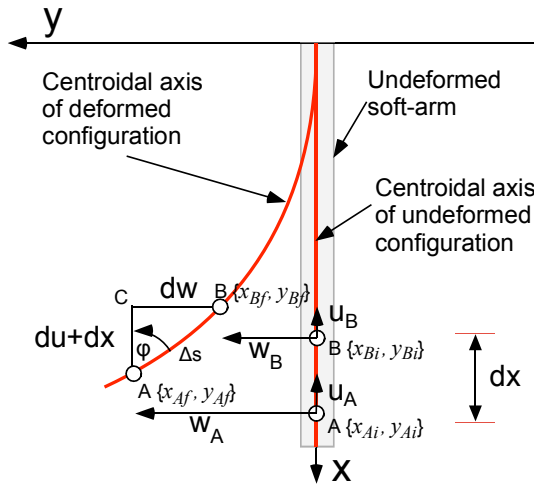


Fig. 4: Graph depicting reference and deformed configurations and the variables that describe the deformation.

Using the Pythagorean theorem on triangle ABC in Fig. 4, and after dividing by dx , results in:

$$\left(\frac{ds}{dx}\right)^2 = \left(\frac{du}{dx} + 1\right)^2 + \left(\frac{dw}{dx}\right)^2 \quad (13)$$

$$ds = \sqrt{\left(\frac{du}{dx} + 1\right)^2 + \left(\frac{dw}{dx}\right)^2} dx \quad (14)$$

where ds is the infinitesimal fiber length in the deformed state along the centroidal axis, and dx is the corresponding infinitesimal fiber length at the undeformed state.

From Fig. 4 and the definition of tangent, the following relationship is derived:

$$\frac{dw}{dx} = \tan(\phi) \left(\frac{du}{dx} + 1\right) \quad (15)$$

Due to conservation of mass for the infinitesimal element, the following is also true:

$$\rho(s)ds = \rho_0 dx \quad (16)$$

where ρ_0 is the mass distribution per unit length in the undeformed case and is assumed constant. Equations (14) and (16) compose the mapping from the deformed space to

the undeformed. This mapping will be used next to change variables from s to x in (6)-(8), and express all differential relationships with respect to the undeformed variable x .

Performing the change of variable, using (14), (16) into (6) - (8), results in:

$$\frac{dQ}{dx} = -T_1 \frac{d\phi}{dx} - T_2 \frac{d\phi}{dx} - N \frac{d\phi}{dx} - \sin(\phi) \rho_0 g \quad (17)$$

$$\frac{dN}{dx} = -\frac{dT_2}{dx} - \frac{dT_1}{dx} + Q \frac{d\phi}{dx} + \cos(\phi) \rho_0 g \quad (18)$$

$$\frac{dM}{dx} = \left(\frac{dT_2}{dx} - \frac{dT_1}{dx}\right) R_c + Q \frac{du}{dx} + 1 \sqrt{(1 + \tan^2(\phi))} \quad (19)$$

D. ODEs relating force N , moment M and strain ϵ

The six ODEs that have been derived up to this point are (1) for $i = 1, 2$, (15) and (17-19). Two more ODEs are required in order to solve for the 8 unknowns. The additional equations are found by establishing relationships between the axial force N , the bending moment M and the strain ϵ .

For the large strain problem it is necessary to use the Cauchy Tensor from which the Green-Lagrange large strain ϵ , is defined as:

$$\epsilon = \frac{1}{2} \frac{ds^2 - dx^2}{dx^2} \quad (20)$$

Since, this expression is true for the centroidal axis, it is also true for all fibers parallel the centroidal axis. It is a strain relationship that can be expressed as $\epsilon(x, z)$, where z is the distance from the centroidal on a cross-section in the undeformed state. The constitutive equation relating stress and strain is given by [17]:

$$\sigma(x, z) = E \epsilon(x, z) \quad (21)$$

Using (14) to (21) results in:

$$\epsilon(x, z) = \frac{du}{dx} + \frac{1}{2} \left(\frac{du}{dx}\right)^2 + \frac{1}{2} \left(\frac{dw}{dx}\right)^2 \quad (22)$$

It is also known that the axial force N , by setting $z = 0$ is given by [17]:

$$\frac{N(x)}{AE} = \epsilon(x, 0) \quad (23)$$

where A is the cross section of the soft arm and is assumed constant, and E is an equivalent Young modulus of the structure. Using (15) to substitute for the term $\left(\frac{dw}{dx}\right)^2$ in (22), and then substituting the updated (22) in (23), yields an expression for $N(x)$:

$$\frac{N(x)}{AE} = \frac{du}{dx} + \frac{1}{2} \left(\frac{du}{dx}\right)^2 + \frac{1}{2} \left(\tan(\phi) \left(\frac{du}{dx} + 1\right)\right)^2 \quad (24)$$

The next step is the derivation of the final ODE by relating the bending moment to the derivatives $du/dx, d\phi/dx$. The bending moment is given by the surface integral:

$$M(x) = \int_A E \epsilon(x, z) z dA \quad (25)$$

Using (22) yields:

$$\begin{aligned} \frac{M(x)}{EI} &= -\frac{d\phi}{dx} \cos(\phi) - \frac{du}{dx} \frac{d\phi}{dx} \cos(\phi) - \\ &\quad \frac{d\phi}{dx} \frac{\sin^2(\phi)}{\cos(\phi)} \left(\frac{du}{dx} + 1\right) \end{aligned} \quad (26)$$

where I is the cross section moment of inertia.

The system of eight non-linear ODEs is composed by (1 for $i = 1, 2, 24, 26, 15, 18, 17,$ and 19), all expressed as a function of x . After several algebraic manipulations, which for economy of space are not presented in this paper, the eight ODEs are decoupled and brought in a form $\frac{dx}{ds} = \mathbf{A}(x)\mathbf{x} + \mathbf{b}(x)\mathbf{u}$, where \mathbf{u} is the force of gravity, so that they can be numerically integrated using a standard ODE solver.

Numerical integration will solve for all 8 unknowns $T_1, T_2, M, Q, N, \phi, u, w$ successively, for every integration step along the discretized centroidal axis.

IV. NUMERICAL SOLUTION AND SIMULATIONS

A. Solving for the Boundary Conditions

The boundary conditions (BC) of the ODE system are the $M(0), Q(0), N(0), \phi(0), u(0), w(0)$ at the soft-arm cross section at the mounting base, as shown in Fig. 3, plus the values of the two tendon tensions $T_1(0), T_2(0)$ generated by the servomotors. The BC values are:

$$u(0) = 0 \quad (27)$$

$$w(0) = 0 \quad (28)$$

$$\phi(0) = 0 \quad (29)$$

$$M(0) = -(T_1(0) - T_2(0))R_c + IW \quad (30)$$

$$Q(0) = 0 \quad (31)$$

$$N(0) = -T_1(0) - T_2(0) + W \quad (32)$$

Equations (27 - 32) state that the centroid of the cross-section of the soft-arm at the mounting base exhibits no deformation. All values of BC are known except $M(0)$ in (30), which cannot be determined unless the offset l of the CM from the vertical x axis is known (see Fig. 3). However, l is not known before the ODE is solved. In order to find the value of l , the iterative algorithm shown in Fig. 5 was executed.

B. Experimental parameter estimation

To provide realistic simulations, the authors opted for model parameter values that correspond to an actual soft-arm. To this end, the estimated parameter values correspond to the physical properties of the modules of the I-Support 2-module soft-arm illustrated in Fig. 6, designed and developed by SSSA [18]. The soft-arm system comprises two soft-arm modules serially connected, where each module is actuated by three tendons and three pneumatic actuators; the tendon actuation in each module is decoupled by design, i.e. the tendons of the distal module do not pass through the proximal module. The soft-arm backbone of each module comprises the three hyperelastic chambers of the pneumatic actuators supported by a flange-type structure (see Fig. 7). In the present paper, only the tendon actuation is used, therefore the pneumatics chambers are constantly at atmospheric pressure. The end-effector position and orientation (tip of distal module) is tracked by a 6DOF magnetic tracker, the TrakStar by Ascension. In Fig. 6, the soft-arm hangs vertically and therefore is also subjected to gravitational force, which is the

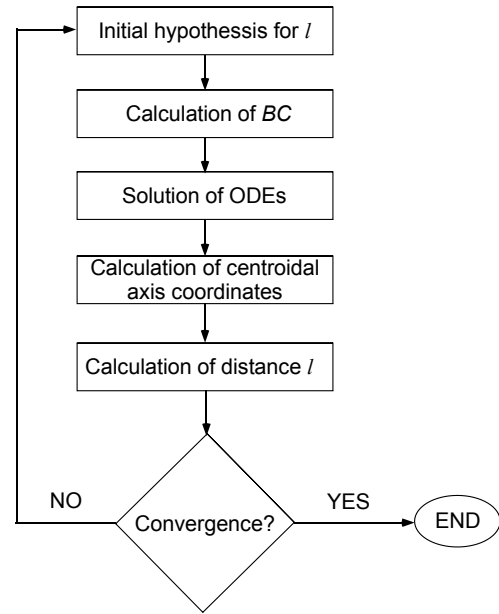


Fig. 5: Flow diagram of the functional iteration for finding the value of distance l .

only external force for the present analysis. In the following sections, the analysis and the experiments are carried out for a one-segment robot, nonetheless they can be generalized to the two segments or more.

1) *Experimental estimation of EI, AE*: A set of 31 experiments were conducted, where in each of them the segment was actuated by a tendon force of different magnitude. The EP (experimental measurement of tips position) was measured and for the same tendon force, the corresponding SP (simulation measurement of tips position) was measured. For every single pair of EP and SP the optimization algorithm satisfies the following objective:

$$\underset{P}{\text{minimize}} \quad J = \|EP - SP\| \quad (33)$$

where P (parameter vector) is given by:

$$P = [AE \ EI] \quad (34)$$

The outcome is the value of P that minimizes the error for every single experiment, therefore there are 31 different

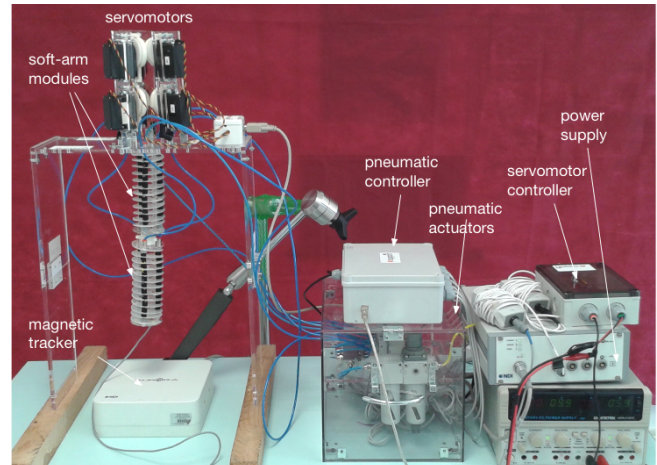


Fig. 6: Experimental set-up of I-Support soft-arm.

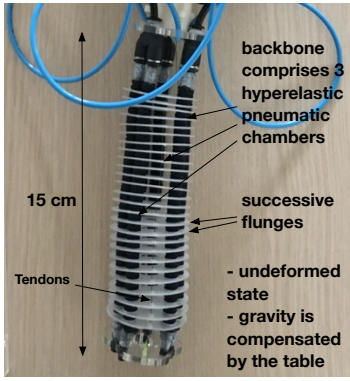


Fig. 7: Single module of soft-arm.

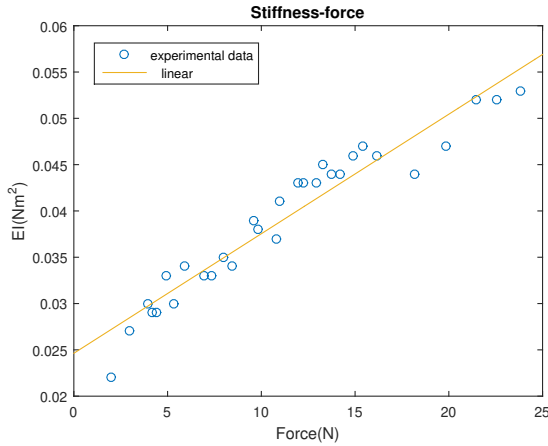


Fig. 8: Relationship between EI and tendon force T , revealed by the identification experiments of the 31 trials.

values of P . For the set of the EI data, a least square algorithm has been applied. Interestingly, the term EI varies as a function of tension T , which in this experiment is proportional to bending moment M . The term EI increases linearly with T according to:

$$EI = 0.0013T + 0.025 \quad (35)$$

The behavior described in (35) is due to the heterogeneous structure of the pneumatic chamber which resembles a compression spring having coils of different pitch. As the compression increases, more spring coils come into contact and less springs are free to deform thus its equivalent stiffness increases. This also holds true for many types soft-arm designs where hyperelastic material are blended with stiffer support structures, and should be taken into account when modeling these soft-arms and control their deformation. It is found that AE varies as a function of tension T , according to the fifth order polynomial:

$$AE = 0.0026T^5 - 0.17T^4 + 3.5T^3 - 20T^2 + 81T + 42 \quad (36)$$

Equations (35) and (36) apply to the case of single tendon actuation. When multiple tendons are actuated, the expressions for EI and EA involve all T_i values, where subscript i refers to the specific tendon i , and are determined following an approach similar to the single tendon case.

C. Simulation results

Indicative 2D simulations of the large strain model, for a single segment soft-arm actuated by two tendons are run for three loading conditions : $\{T_1 = 20N, T_2 = 10N\}$, $\{T_1 = 30N, T_2 = 10N\}$, $\{T_1 = 40N, T_2 = 10N\}$. The values of the other parameters of the simulation are $L = 0.15m$, $R_c = 0.03m$, $mass = 0.14kg$. The results are shown in Fig. 9. The origin of the axis is located in the upper right corner of the plot, like in Fig. 2.

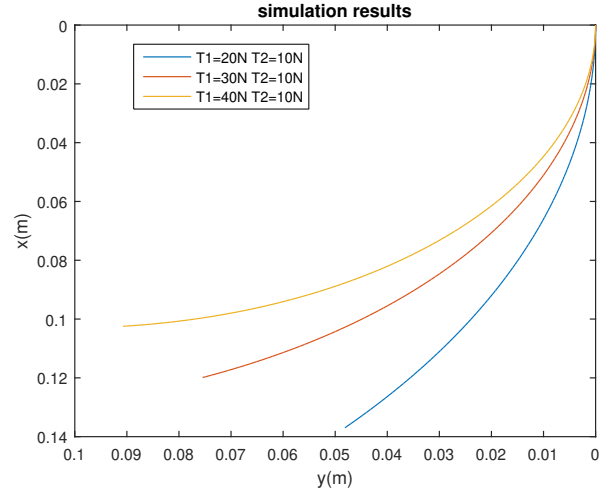


Fig. 9: Single module, simulation results for 3 actuation pairs.

V. EXPERIMENTAL VALIDATION

The large strain model is validated using a single segment tendon-driven soft-arm. The experimental set-up is the one shown in Fig. 6. The experiment involved the deformation of the segment by activating one out of the three tendons so that the soft arm executes a curved motion on a vertical plane (with the effect of gravity). Eight trials were conducted for eight different input tendon commands. For each trial, the tendon force was measured and the $x-y$ position of the tip of the soft arm was recorded by the magnetic tracker. The measurements and the corresponding simulation results are presented and compared in Table I. It is seen that the maximum end-point error is $7mm$, which corresponds to 4% max error in the prediction of the soft-arm tip position. This result indicates the validity of the large strain model.

Next, the large-strain model is used to predict the deformation of the soft-arm when it is actuated by the right tendon tension equal to $T_1 = T = 9.6N$ ($T_2 = 0N$), without the effect of gravity. Fig. 10 compares simulation results and experimental measurements of the soft-arm geometry. The circles designate the measurement of the position of each flange of the soft-arm, and the dashed line the simulation results. The max error is around 4%. This experiment demonstrates that not only does the model predict accurately the tip deflection, but also captures equally well the shape of the soft arm.

The ability to predict the shape of the structure offered by the large-strain model is especially important in applications where the entire soft structure must be leveraged, for example when the arm is moving in confined spaces or when whole

TABLE I: Comparison of experimental and simulation results

<i>Tension</i> [N]	x_{sim} [m]	y_{sim} [m]	x_{exp} [m]	y_{exp} [m]	<i>Error norm</i> [m]
2.73	0.1429	0.0279	0.1439	0.0296	0.002
3.47	0.1409	0.0343	0.1409	0.0343	0.0001
6.69	0.1312	0.0603	0.1332	0.0662	0.006
6.94	0.1304	0.0583	0.1324	0.0629	0.005
7.43	0.1288	0.0610	0.1318	0.0643	0.004
7.93	0.1272	0.0636	0.1252	0.0671	0.004
9.66	0.1213	0.0717	0.1243	0.0768	0.006
10.9	0.1170	0.0765	0.1210	0.0800	0.005

arm manipulation is desirable. In the aforementioned experiments the only external force exerted on the soft-arm was the force of gravity. The authors plan to conduct experiments with concentrated external loads as future work, where a new set of boundary conditions will be defined and the problem will be solved again iteratively.

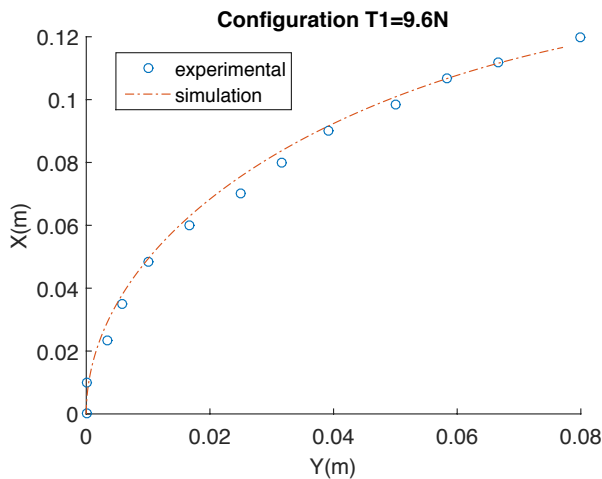


Fig. 10: Comparison of simulation and experimental measurements of the soft arm shape, for tendon actuation $T = 9.6N$.

VI. CONCLUSION

This paper presented the mathematical derivation and experimental validation of a computational model that accurately predicts static, non-linear large-strain deformations of tendon driven non-slender soft-arm manipulators subjected to gravity. No simplifying assumptions on the curvature of the structure were made on the degree of stretching or compression increasing this way the accuracy and generality of the model. Furthermore the paper proposed an iterative method for solving numerically the resultant non-linear system of coupled differential equations and different simulation scenarios were demonstrated. The model was experimentally validated on an experimental set-up comprising one segment of the I-Support soft-arm, and which integrates stretchable and compressible hyperelastic (rubber-type) materials in its non-homogeneous back bone structure.

ACKNOWLEDGMENT

The authors would like to thank Mariangela Manti, Matteo Cianchetti and Cecilia Laschi from SSSA, Pontedera, Italy, for providing the I-Support soft-arm set-up, and Prof. Costas Tzafestas and Thanasis Dometios at ICCS-NTUA, Athens, Greece, for their support during the experiments.

REFERENCES

- [1] M. Cianchetti, C. Laschi, A. Menciassi, and P. Dario, "Biomedical applications of soft robotics", *Nature Reviews Materials*, vol. 3, no. 6, 2018, pp. 143-153.
- [2] P. Polygerinos et al., "Soft Robotics: Review of Fluid Driven Intrinsically Soft Devices; Manufacturing, Sensing, Control, and Applications in Human Robot Interaction", *Advanced Engineering Materials*, vol. 19, no. 12, December 2017.
- [3] A. D. Marchese, R. Tedrake and D. Rus, "Dynamics and trajectory optimization for a soft spatial fluidic elastomer manipulator", *International Journal of Robotics Research*, 2016, vol. 35, no. 8, pp. 1000-1019.
- [4] <http://www.i-support-project.eu/>
- [5] R. J. Webster III and B. A. Jones, Design and kinematic modeling of constant curvature continuum robots: A review, *Int. J. of Robotics Research*, 2010, vol. 29, pp. 1661-1683.
- [6] G. S. Chirikjian and J. W. Burdick, "Kinematically optimal hyper-redundant manipulator configurations", *IEEE Transactions on Robotics and Automation*, vol. 11, no. 6, 1995, pp. 794-806.
- [7] M. Rolf and J. J. Steil, "Constant curvature continuum kinematics as fast approximation for the Bionic Handling Assistance," *IEEE International Conference on Intelligent Robots and Systems (IROS)*, Vilamoura, Portugal, October 2012.
- [8] Habibi, Hossein ; Kang, Rongjie ; Walker, Ian D. ; Godage, Isuru S. ; Branson, David. "Developing a 3-D. Lumped Mass Model to Present Behaviour of Large Deformation Surface Based Continuum Robots," *IUTAM Bookseries, Springer, Cham: Zahariev E., Cuadrado J. (eds) IUTAM Symposium on Intelligent Multibody Systems Dynamics, Control, Simulation. Vol. 33 2019. pp. 133-147*
- [9] D.B. Camarillo, C.F. Milne, C.R. Carlson, M.R. Zinn, J.K. Salisbury. "Mechanics modeling of tendon-driven continuum manipulators". *IEEE Transactions on Robotics*; 2008, 24: pp.1262-1273.
- [10] F. Renda and L. Seneviratne, "A Geometric and Unified Approach for Modeling Soft-Rigid Multi-Body Systems with Lumped and Distributed Degrees of Freedom," *2018 IEEE International Conference on Robotics and Automation (ICRA)*, Brisbane, QLD, 2018, pp. 1567-1574.
- [11] V. Falkenhahn, T. Mahl, A. Hildebrandt, R. Neumann, O. Sawodny, "Dynamic Modeling of Bellows-Actuated Continuum Robots Using the Euler-Lagrange Formalism", *IEEE Transactions on Robotics*, vol. 21, no 6, December 2015.
- [12] F. Renda, M. Cianchetti, M. Giorelli, A. Arienti, and C. Laschi, "A 3d steady-state model of a tendon-driven continuum soft manipulator inspired by the octopus arm", *Bioinspiration and Biomimetics*, 2012, vol. 7, no 2, p. 025006.
- [13] D. C. Rucker, B. A. Jones, and R. J. Webster, III, "A Geometrically Exact Model for Externally Loaded Concentric-Tube Continuum Robots", *IEEE Transactions on Robotics*, vol. 26, no. 5, October 2010, pp. 769-780.
- [14] P. Sears and P. E. Dupont, "A steerable needle technology using curved concentric tubes," in *Proc. IEEE/RSSJ Int. Conf. Intell. Robots Syst (IROS 2006)*, 2006, pp. 2850-2856.
- [15] I. A. Gravagne, C. D. Rahn, and I. D. Walker, "Large-deflection dynamics and control for planar continuum robots," *IEEE/ASME Trans. on Mechatronics*, Jun. 2003, vol. 8, pp. 299-307.
- [16] Bieze, T. M., Largilliere, F., Kruszewski, A., Zhang, Z., Merzouki, R., and Duriez, C., "Finite Element Method- Based Kinematics and Closed-Loop Control of Soft," *Continuum Manipulators. Soft robotics*, 2018, 5(3), pp. 348-364.
- [17] F. P. Beer and E. R. Johnston Jr. *Vector Mechanics for Engineers: Statics*, 3rd edition, McGraw-Hill Ryerson, 1995.
- [18] M. Manti et al. (2017), "Exploiting Morphology of a Soft Manipulator for Assistive Tasks", in: Mangan M., Cutkosky M., Mura A., Verschure P., Prescott T., Lepora N. (eds) *Biomimetic and Biohybrid Systems. Living Machines 2017*. Lecture Notes in Computer Science, vol 10384. Springer, Cham.